IEEE Robotics and Automation Letters (RA-L) paper, presented at ICRA 2024, Yokohama, Japan. Cite as RA-L paper.

Interaction Control for Tool Manipulation on Deformable Objects Using Tactile Feedback

Hanwen Zhang, Zeyu Lu, Wenyu Liang, Haoyong Yu, Yao Mao, and Yan Wu

***Abstract*—The human sense of touch enables us to perform delicate tasks on deformable objects and/or in a vision-denied environment. To achieve similar desirable interactions for robots, such as administering a swab test, tactile information sensed beyond the tool-in-hand is crucial for contact state estimation and contact force control. In this paper, a tactile-guided planning and control framework using GTac, a hetero*G*eneous *Tac*tile sensor tailored for interaction with deformable objects beyond the immediate contact area, is proposed. The biomimetic GTac in use is an improved version optimized for readout linearity, which provides reliability in contact state estimation and force tracking. A tactile-based classification and manipulation process is designed to estimate and align the contact angle between the tool and the environment. Moreover, a Koopman operator-based optimal control scheme is proposed to address the challenges in nonlinear control arising from the interaction with the deformable object. Finally, several experiments are conducted to verify the effectiveness of the proposed framework. The experimental results demonstrate that the proposed framework can accurately estimate the contact angle as well as achieve excellent tracking performance and strong robustness in force control.**

***Index Terms*—Force and tactile sensing, force control, contact modeling.**

I. Introduction

With the advancement of robotics and automation technologies, robots have become an effective and important solution to automate standard processes, assist humans, or even relieve them from mundane tasks. The use of robots can speed up the process, improve accuracy, reduce operating costs, and avoid human exposure to dangerous environments. During the COVID-19 pandemic, many robots and automation systems were developed and deployed to deal with the challenges posed by the pandemic [1], [2]. Notably, some of these applications require volumetric episodes of contact with human body or soft tissues. One well-known example is the swab test.

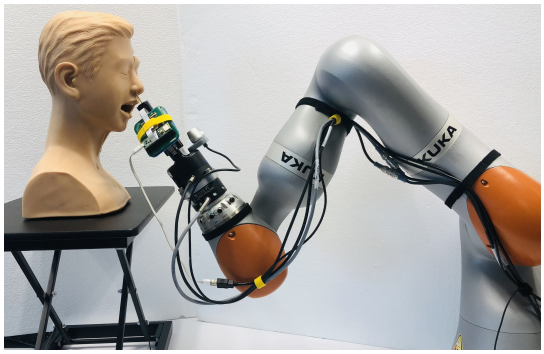

Fig. 1. Illustration of a robotic setup for nasal swab test.

Manipulating soft tissues on the human body poses a significant challenge due to their deformable nature. The presence of strong nonlinearities, viscoelasticity and uncertainty makes it complex for robust and precise interaction control in such environment. Moreover, applications such as the swab test require the robot to operate in vision-denied or heavily occluded conditions, which also adds to the challenges for robot deployment. Fig. 1 shows an illustration of a robotic system for nasal swab test. The robot is to hold a cotton swab and collect samples from the human nasal cavity. To ensure the successful, safe, and efficient collection of a sample, the swab head must maintain a good contact with the soft and deformable walls of the nostril. Notably, as the nasal cavity is a confined space, effective visual perception is challenging while addressing all of the aforementioned challenges is essential for successful robotic swab testing.

Taking the robotic swab test as a reference point, this paper aims to investigate and address the challenges of *enabling a robot to perform a desired interaction with a deformable object, such as the human body, without visual cues*. According to [3], touch sensing and feedback control can be deduced as the two essential elements for successful and safe swabbing. The combination of these two key elements can help a robotic swab operator achieve alignment planning to ensure the swab is parallel to the nasal wall and contact force control to maximize contact with the nasal wall while maintaining a gentle contact force to minimize discomfort and injury.

Inspired by this process, the idea of using tactile sensors and feedback control is proposed to solve the aforementioned problems in this paper. Firstly, a tactile sensor with a compact

Manuscript received: September 27, 2022; Revised January 18, 2023; Accepted February 20, 2023. This paper was recommended for publication by Editor Ashis Banerjee upon evaluation of the Associate Editor and Reviewers' comments. This work was supported by the A*STAR Career Development Fund (Grant No.: C210812049). Hanwen Zhang and Zeyu Lu contributed equally in this work. *(Corresponding author: Wenyu Liang)*

Hanwen Zhang, Wenyu Liang and Yan Wu are with the Institute for Infocomm Research (I^2R), Agency for Science, Technology and Research (A*STAR), Singapore. Hanwen Zhang is also with the Key Laboratory of Optical Engineering, Chinese Academy of Sciences, Chengdu, China 610209, the Institute of Optics and Electronics, Chinese Academy of Sciences, Chengdu, China 610209, School of Electrical, Electronic and Communication Engineering, and the University of Chinese Academy of Science, Beijing, China 100039 (e-mail: hanwenzhang1996@hotmail.com; liang_wenyu@i2r.a-star.edu.sg; wuy@i2r.a-star.edu.sg).

Zeyu Lu and Haoyong Yu are with the Department of Biomedical Engineering, National University of Singapore, Singapore 117576 (e-mail: zeyu.lu@u.nus.edu; bieyhy@nus.edu.sg).

Yao Mao is with the Key Laboratory of Optical Engineering, Chinese Academy of Sciences, Chengdu, China 610209, and the Institute of Optics and Electronics, Chinese Academy of Sciences, Chengdu, China 610209 (e-mail: maoyao@ioe.ac.cn).

IEEE Robotics and Automation Letters (RA-L) paper, presented at ICRA 2024, Yokohama, Japan. Cite as RA-L paper.

yet flat form factor, robust repeatability, sufficient sensing range and frequency is needed. The GTac [4], a biomimetic hetero**G**eneous **Tac**tile sensor originally designed to localize and grasp objects [5], has many of the aforementioned properties. To improve the sensor readout linearity for better estimation of the contact states and to infer contact angle on the fly, some changes are made to the GTac. The new version also provides the spatial resolution alongside the existing temporal one for feedback necessary for real-time control.

Various works [6]–[10] have been conducted to address the challenges of interaction/contact force control on deformable/soft objects. In [6], a linear model based on viscoelastic behaviour and contact effect is built to represent the mapping of interaction between a soft membrane and a rigid tool set with an optimal controller designed. In [7], a force regulation controller via admittance controller is designed for grasping control of fragile and deformable objects. In [8], a Hunt–Crossley model-based force controller is developed for soft tissue interaction, following the state feedback regulation and active observer techniques. In [9], a force controller is proposed for the stable grip control on soft objects with time-varying stiffness. In [10], a neural network-based learning controller with an adaptive compensator is proposed to deal with tool-soft tissue interaction. These works address the interaction nonlinearity by either linearizing the model-based control or directly applying nonlinear control. However, the restricted accuracy of the linearized models limits the performance of the first control methods, while the nonlinear controller is complex to design and implement.

To address the challenges in the controller design for robot-deformable/soft object interaction, the use of Koopman operator [11] is considered. The key idea of Koopman operator is to embed a nonlinear finite dimensional autonomous dynamical system into an infinite dimensional linear system. In practice, the Koopman operator is approximated as a finite dimensional linear operator using a data-driven approach, without requiring prior knowledge of the dynamical system. Recently, several practical algorithms have been developed for approximating Koopman operators into finite dimensional space called Koopman embedded space [12], [13], making Koopman operator a commonly-used tool for spectral and stability analysis [14], [15]. To solve the limitation that Koopman operator does not accept input signal by its original structure, several attempts extend Koopman operators into actuated systems, especially control systems [16]–[19]. In [17] and [20], they show that the Koopman operator is successfully work with optimal control technique in robotics. Leveraging on its advantages, in this paper, we design a Koopman operator to accurately approximate the nonlinear soft interaction dynamics, and propose a linearized model-based optimal control for precision robotic interaction control.

This paper proposes and develops a tactile-guided motion planning and interaction control framework for tool manipulation on deformable objects. The framework comprises two parts: tactile-based contact angle alignment and Koopman operator-based optimal contact force control. The main contributions of this paper are as follows: i) design of a tactile perception and manipulation planning process to estimate and align the angle between the tool and the contacting object, which is beyond the direct contact of the sensor; ii) development of a contact force controller using Koopman operator and optimal control technique for deformable objects with nonlinearities present during interaction; and iii) design and integration of an improved version of GTac, a biomimetic tactile sensor, with a robotic system to close the tactile-robot action loop.

The rest of this paper is organized as follows. Section II describes the robotic system, the tactile sensor design, the interaction task and the overall framework. Section III presents the manipulation planning process for contact angle alignment. The Koopman operator-based modeling and control scheme is designed in Section IV. Section V shows the experimental results of the proposed framework using a robot manipulator. Finally, conclusions are drawn in Section VI.

II. System, Task, and Framework Descriptions

The system setup shown in Fig. 2 consists of a KUKA LBR iiwa 14 R820 robot manipulator, a Robotiq 2F-85 two-finger gripper, and a GTac tactile sensor. The robot manipulator has 7-degrees-of-freedom (7-DoF) and provides fast and accurate movements. The gripper is mounted on the mounting flange of the robot manipulator (on axis 7), and a GTac sensor is attached to one side of one gripper's finger. A swab is held by the gripper, and the GTac sensor is used to capture the interaction between the swab and the deformable object/environment.

To simulate the human tissue-like deformable environment with varying tissue thickness for experiments and evaluation, a number of soft mock-up films with different thickness are fabricated. The soft films are made of a silicone material (Dragon Skin^{TM} 30) with a 100% modulus of 0.593 MPa [21] that has close characteristics to the human tissue (for instance, lateral nasal cartilage: Young's modulus ranges from 0.69 to 1.27 MPa [22], human skin: Young's modulus varies from 0.06 to 0.85 MPa [23]). Three films with the same material but different thicknesses of 1.8 mm, 2.7 mm, and 4.0 mm are used, which are named as "thin" soft film, "original" soft film, and "thick" soft film, respectively. Remarkably, the "original" soft film is 1.5 times thicker than the "thin" one while the "thick" one is 1.5 times thicker than the "original" one.

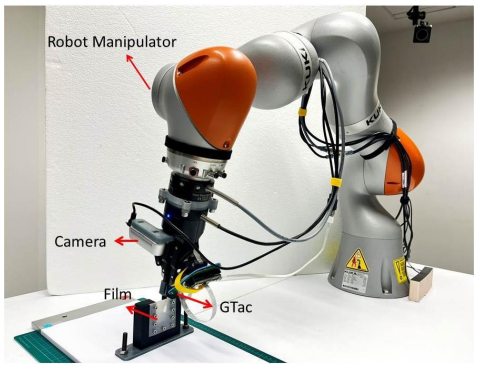

Fig. 2. Robotic system setup with the GTac sensor.

IEEE Robotics and Automation Letters (RA-L) paper, presented at ICRA 2024, Yokohama, Japan. Cite as RA-L paper.

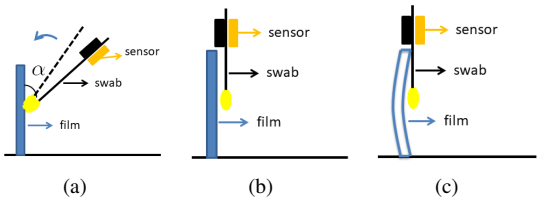

Fig. 3. Working process of the interaction task: (a) Step 1: initial contact state after touch; (b) Step 2: angle alignment (parallel to the contact surface); (c) Step 3: sample collection by applying desired contact force.

A. Interaction Task and Overall Framework

Considering the robotic swab test (where the alignment and desired contact are needed) as the example in this paper, there are three steps to process the swab test by the robot, as shown in Fig. 3. Step 1: the robotic system holds the swab to approach to the target deformable object (e.g., nasal cavity, skin). This step can be done by a vision-guided manipulation planning. Step 2: the swab is manipulated to align with the contact surface (to maximize the contact area). Step 3: the swab applies the desired force (and rotational motion) on the contact surface to collect the sample. Note that Steps 2 and 3 may be conducted in a vision-denied environment due to limited access for vision system in an enclosed confined space.

Step 1 is assumed as out of scope in this work. The main focus is to develop a planning and control framework for the robotic system to automatically carry out the last two steps where no visual cue is available. The proposed overall framework is described in Fig. 4, where a tactile-based manipulation planning process (for contact angle alignment) and a Koopman operator-based control scheme (for contact force tracking) are designed for Steps 2 and 3, respectively. A switch mechanism is designed in this framework to manage the working sequence of Steps 2 and 3 via the switching index.

B. GTac Sensor

The improved design of the GTac sensor is shown in Fig. 5. The GTac sensor is a biomimetic tactile sensor with skin-like heterogeneous force feedback from its flat surface. It consists of 4×4 piezoresistive sensing array with a resolution of 2.5 mm per point (extrinsic FA-I layer) and a Hall-effect sensing element (intrinsic SA-II layer) and can acquire multimodal tactile feedback including normal and shear contact forces. The 16 taxels are evenly distributed on its surface to provide the magnitude and distribution of the normal contact forces. The GTac sensor also provides a global 3D contact force including normal and shear force. Significantly, the FA-I layer senses the contact configurations while the SA-II layer measures the

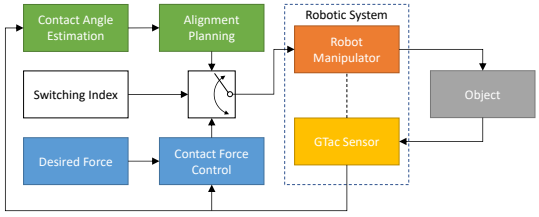

Fig. 4. Block diagram of the proposed overall framework.

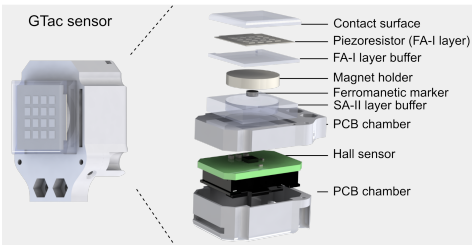

Fig. 5. Design of the GTac sensor integrated into the gripper.
† GTac sensor web page: https://roobooot.github.io/GTac_/

contact force in 3D accurately. In summary, the GTac sensor has 19 tactile sensing outputs (16 from the FA-I layer and 3 from the SA-II layer) which include the normal force F_z, tangential force F_x and F_y of a single-point measurement as well as the normal forces of the 16 points.

The original GTac† sensor [4] was designed to provide stable grasping of objects. In this work, the GTac sensor is improved along the task requirements. The main improvements are on adding the FA-I layer buffer and the compact packaging. The FA-I layer buffer enhances the signals linearity by balancing the pressure distribution between the piezoresistors and rigid magnet holder. The softness of both sides of the FA-I layer would increase the evenness of how the pressure being distributed on the surface of the piezoresistors. Furthermore, the arrangement of the electrical and mechanical components is optimized inside the GTac sensor so that it is more compact for easy integration into the gripper.

III. Tactile-Based Contact Angle Alignment

As no visual information is available, to achieve the angle alignment between the tool (i.e., swab) and the contact surface, a "touch, judge, and align" manipulation planning process based on tactile information is proposed. In this process, a touch action via position control (fixed displacement) is applied on the contact surface by the swab and the corresponding tactile feedback is recorded at the handle side of the swab by the GTac sensor. Significantly, as the contact area, pressure distribution, and the torque amplitude vary with different contact angles, it is possible to use the GTac sensor's tactile information to estimate the current contact angle. Then, based on the recorded tactile data and the ground truth of contact angle provided by robot proprioception, a supervised learning approach can be employed to establish the correlation between the angle and the tactile reading. Finally, an alignment motion is planned and executed according to the estimated angle. The manipulation planning process can be repeated until the angle is within an acceptable range.

In this paper, the angle estimation problem is formulated as a classification problem where different angles can be defined as different class labels. Depending on the resolution requirement, by solving this classification problem, the system is able to figure out the correct angle subject to the current contact situation. Because swab test usually prefers larger area of contact with the swabbing surface, a small range of angles from 0 to 0.5 rad with uniform intervals of 0.025 rad are set.

A. Preliminary Study on Tactile Data for Angle Estimation

To design and train the classifier, a total of 420 sets of tactile data are collected while the swab is contacting with the three different soft films (see Fig. 2 and Fig. 3) under different contact angles. Each dataset contains 19 dimensions of tactile sensing information from the GTac sensor.

Two sets of raw tactile data with 19 dimensions of each while the contact angle are 0 rad and 0.225 rad are shown in Fig. 6. By comparing these two data visually, it can roughly distinguish the data differences. Significantly, for different angles, the differences of the datasets mainly appear in the data from the FA-I layer. Therefore, it can be inferred that contact angle classification via the tactile data is feasible.

To further analyze the dataset, principle component analysis (PCA), an unsupervised machine learning algorithm for exploring high-dimensional data structures, is applied to the collected tactile data. The experimental results of PCA on the tactile dataset are shown in Fig. 7. The results on the distribution of the eigenvalues from PCA shows that after dimensionality reduction, 94.8% of the data information can be visualized in the feature space with top three features. Thus, it further verifies that using the tactile data contains the information for angle estimation.

Based on the above observations, statistical classification model is proposed to construct the contact angle classifier in this paper. Here, three potential classification models, namely linear discriminant analysis (LDA), quadratic discriminant analysis (QDA), and support vector machine (SVM) are chosen as the classifier candidates. Then, a comparison study for the classifier selection will be carried out with a five-fold cross validation in Section V-A.

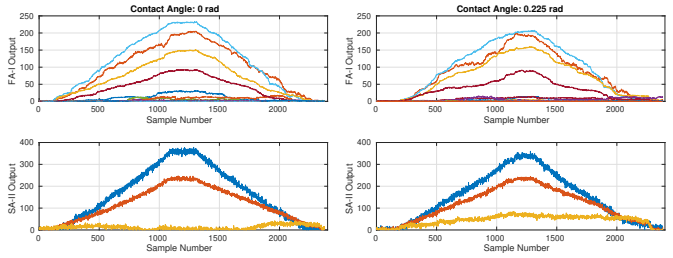

(a) (b)

Fig. 6. Raw tactile data of different contact angles: (a) 0 rad; (b) 0.225 rad.

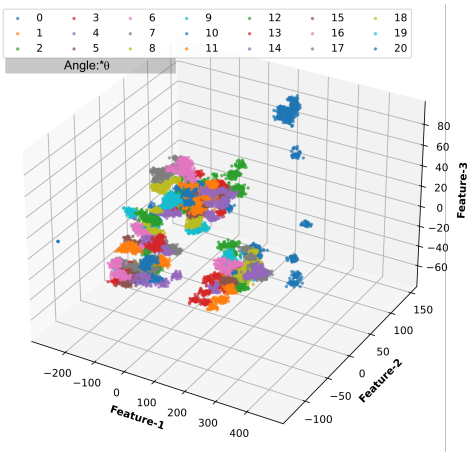

Fig. 7. Data visualization in the top three variance features obtained by PCA for the contact angle dataset.

B. Contact Angle Alignment

The goal of the contact angle alignment is to ensure full contact between the swab and the contacting surface. In other words, the contact angle should be as small as possible, preferably equal to zero. With the estimated angle $\hat{\alpha}$ obtained by the classification model with the recorded tactile data, a desired angle ϕ_r is set as $\phi_r = \bar{\phi} - \hat{\alpha}$, where $\bar{\phi}$ is the current angle between the GTac sensor surface and the x-z plane of the object's coordinate system.

This desired angle is then sent to the robot controller to set the target pose for the robot manipulator. Finally, the robot manipulator will pivot its end-effector (around the end-point of the swab) to the desired angle according to the target pose input via its built-in inverse kinematics solver and joint position controller so as to achieve the angle alignment.

IV. Koopman Operator-Based Optimal Contact Force Control

Once the required contact angle alignment is achieved, another important process is to apply a desired contact force reference/trajectory to the object for a successful procedure. In this paper, an interaction model based on Koopman operator is proposed to linearize the nonlinear model of deformable object interaction so that linear control techniques can be easily applied to such a nonlinear system. Then, the optimal control scheme leveraging on the Linear Quadratic Regulator (LQR) is designed to achieve the optimal performance. The proposed control scheme is named as Koopman operator-bsaed Linear Quadratic controller (K-LQ controller).

A. Koopman Operator

Koopman operators is essentially a global linearization of a nonlinear system by a coordinate transformation of the original system. First, the mathematical representation for a general discrete nonlinear system is given by

$$x_{t+1} = G(x_t), x_t \in \mathbb{R}^{N_x}, \tag{1}$$

where $t \in \mathbb{N}$ is time step, G is the state-to-state mapping in the state space $\mathbb{R}^{N_x}$.

Then, define an observation function g,

$$y_t = g(x_t),\ \forall g : \mathbb{R}^{N_x} \to \mathbb{R}^{N_y}, \tag{2}$$

where y_t are the measurable outputs from the dynamical system. Also, define Koopman operator K to be a linear operator acting on an observation function g, where K is infinite-dimensional and satisfies the following conditions:

$$Kg(x_{t+1}) = g(G(x_{t+1})). \tag{3}$$

Here, K describes the value of g as a function of evolution in phase space orbit.

Therefore, the finite-dimensional nonlinear dynamical systems can be characterized by the analysis of the infinite-dimensional linear operator K. Here, observables can be combined into a set of vector-valued observables to compute

IEEE Robotics and Automation Letters (RA-L) paper, presented at ICRA 2024, Yokohama, Japan. Cite as RA-L paper.

the finite-dimensional approximation Koopman operator for nonlinear dynamical systems. The target of the Koopman operator and its finite-dimensional approximation algorithms is to find a function dictionary $\psi : \mathbb{R}^{N_x} \rightarrow \mathbb{R}^{N_\psi}$ and the matrix $\hat{K} \in \mathbb{R}^{N_\psi} \times \mathbb{R}^{N_\psi}$ such that the original dynamical system becomes approximately linear,

$$\begin{cases} \psi(x_{t+1}) = \hat{K}\psi(x_t) + \gamma(x_t) \\ y_t = g(x_t) = b\psi(x_t) \end{cases}, \tag{4}$$

where $\gamma(x_t)$ is the residual approximation error, $\psi(x)$ is a user-defined vector function, and $b \in \mathbb{R}^{N_y} \times \mathbb{R}^{N_\psi}$ is a matrix.

To obtain an explicit expression for the Koopman operator in a finite-dimensional linear space, an invariant subspace of the infinite-dimensional function space containing all the system state variables is obtained by extended dynamic mode decomposition (EDMD).

Remarkably, the idea of input compensation that was originally proposed to learn the autonomous systems from actuated training data is employed to build the interaction model. Assume that the observed dataset is $\{x(n), y(n)\}_{n=1}^{N}$, to find the $\hat{K}$, the below minimization problem is needed to be solved,

$$\hat{K} = \underset{\hat{K} \in \mathbb{R}^{N_\psi} \times \mathbb{R}^{N_\psi}}{\arg\min} J_1(\hat{K}) = \sum_{n}^{N} \|\gamma(x(n))\|^2. \tag{5}$$

From the above equation, the $\hat{K}$ can be solved by

$$\hat{K} = O^{\dagger} V, \tag{6}$$

with $O = \frac{1}{N} \sum_{n=1}^{N} \psi(x(n))^T \psi(x(n))$ and $V = \frac{1}{N} \sum_{n=1}^{N} \psi(x(n))^T \psi(y(n))$, where $O^{\dagger}$ is the pseudo-inverse of O.

B. K-LQ Controller

The classical Koopman theory was developed for autonomous dynamical systems, which is of interest to investigate how it can be extended to systems with inputs. A discrete nonlinear system is given as follows,

$$\begin{cases} x_{t+1} = G(x_t, u_t) \\ y_t = g(x_t) \end{cases}, \tag{7}$$

where $x \in X \in \mathbb{R}^{N_x}, u \in \mathbb{R}^{N_u}$, x is the system output, u is the system input, and G is the system mapping function.

For closed-loop control, an input u_t is generated by the state-dependent control function $u_t = h(x_t)$, i.e.,

$$Kg(x_t, u_t) \triangleq g(G(x_t, u_t), h(x_t, u_t)). \tag{8}$$

The calculation of the Koopman operator for a given closed-loop control law can therefore be reduced to the calculation of the Koopman operator for an autonomous dynamical system.

In a control system with inputs, as shown in (4), the vector function $\psi(x, u)$ is defined as

$$\psi(x, u) = [x^T, u^T, \varphi_1(x, u)^T, ..., \varphi_{N_\psi}(x, u)^T], \tag{9}$$

where $\varphi(x, u)$ is the lifting function to be designed.

By choosing a derivable $\psi(x, u)$, the system can be linearized in the following form,

$$\begin{cases} x_{k+1} \approx \bar{K}^T \dfrac{\partial \psi}{\partial x} x_k + \bar{K}^T \dfrac{\partial \psi}{\partial u} u_k \approx Ax_k + Bu_k \\ y_k = Cx_k \end{cases} \tag{10}$$

where $\bar{K}^T \in \mathbb{R}^{N_x \times N_\psi}$ is the first N_x columns of $\hat{K}$.

With the above linearized system, the LQ technique can be applied because the LQ controller is a simple optimal control method that can realize the calculation of a series of optimal control quantities in a period of time. The LQ technique is to find out a solution by solving a linear-quadratic problem [20]. For the trajectory tracking, its quadratic cost is given by

$$J_2 = \sum_{k=1}^{\infty} [e_k^T Q e_k + u_k^T(t) R u_k], \tag{11}$$

where $e_k = r_k - y_k$ (i.e., $e(t) = r(t) - y(t)$) is the tracking error, r_k (i.e., $r(t)$) is the reference signal (trajectory), Q and R are both positive definite matrices, $Q \in \mathbb{R}^{N_\psi \times N_\psi}$ is in the diagonal form. Q, R are user defined and relate to the convergence speed and the control effort, respectively.

The control law for the trajectory tracking using the LQ optimal control takes the state feedback form [24], which is

$$u_{K-LQ} = -K_k x + K_r v + K_I \int_0^t e d\tau, \tag{12}$$

where K_k and K_r are the optimal control parameters that can be obtained via the LQ optimal control technique with J_2, v is a variable related to r, and K_I is the parameter of the integral control action.

V. Experiments, Results and Discussions

To verify the effectiveness and performance of the proposed motion planning and interaction control framework on deformable objects, experiments are conducted with the three different soft films and the experimental setup shown in Fig. 2. In this setup, both the GTac sensor driver and the robot manipulator controller are connected and communicated to a computer via Robot Operating System (ROS). The sensor data processing, motion planning and interaction control framework are implemented on the computer via MATLAB.

A. Contact Angle Estimation

To estimate the contact angle, the 19 raw tactile signals from the GTac sensor are used as the input of the classifier. The output of the classifier is the estimated angle (from 0 to 0.5 rad interpolated by 21 classes). The collected data used in the preliminary study in Section III-A is also used in the experiments of this subsection. The comparison results among different models are shown in Fig 8. The 420 sets of data collected in section III-A were used in the experiments. Here, 80% of the total data were randomly selected as the training set and 20% as the test set each time. In short, the 5-fold cross-validated results shown in Fig. 8 suggests that QDA outperforms LDA and SVM in terms of accuracy, precision, and recall. Therefore, the QDA is employed for the contact angle estimation.

IEEE Robotics and Automation Letters (RA-L) paper, presented at ICRA 2024, Yokohama, Japan. Cite as RA-L paper.

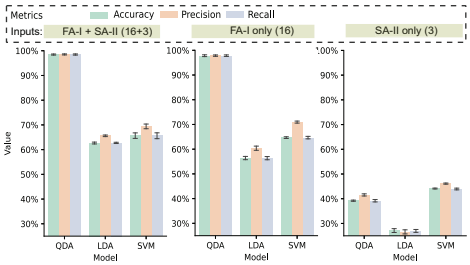

Fig. 8. Comparison results with different inputs among LDA, QDA, SVM.

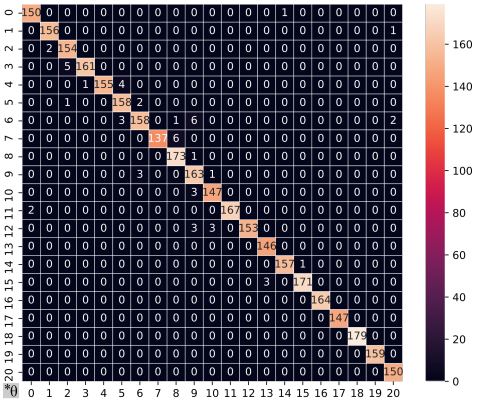

Fig. 9. Confusion matrix of the last fold using the QDA classifier.

Furthermore, comparison in the performance of using different input combinations, i.e., FA-I + SA-II, FA-I only and SA-II only, is also presented in Fig. 8. The results show that full input from the GTac sensor brings the best performance for the angle estimation while FA-I only outperforms SA-II only. This is expected as FA-I input provides spatially localized taxel information based on the deformation changes given an extrinsic force contact as compared to a resultant point-based force reading provided by SA-II.

Finally, the confusion matrix from the test set of the last fold using the QDA classifier with full input, as illustrated in Fig. 9, shows a classification accuracy of 98.4%. In other words, it can be concluded that the proposed contact angle estimation method can well estimate the contact angle with a resolution of up to 0.025 rad (approximately 1.5 deg).

B. Interaction Model Linearization via Koopman Operator

To investigate the relationship between the contact force applied on the deformable object and its deformation, an experiment is carried out while the swab on the gripper is parallel to the object surface. During this experiment, the robot manipulator moves the swab to interact with the film via position control with a designed trapezoidal motion profile, and the contact force is recorded by the tactile sensor. Taking the original film as an example, set the travel distance (x) of the swab as the system input and the z-axis force (F_z) of the tactile sensor as the output, the input-output relationship is depicted in Fig. 10. As can be seen, this relationship exhibits nonlinear characteristics and thus such an interaction can be treated as a nonlinear system. It can also be observed that hysteresis exists during the deformable object interaction.

With the recorded data, the interaction model can be built via the proposed method based on Koopman operator presented in Section IV. Taking $\psi_i^{N_\psi}$ in $\psi(x,u)$ as an N_ψ-th order Legendre expansion, the Koopman operator $\hat{K}$ is constructed from the recorded data, and the linearized system parameters A and B are obtained according to equation (10). Here, the Legendre polynomial is chosen as the lifting function.

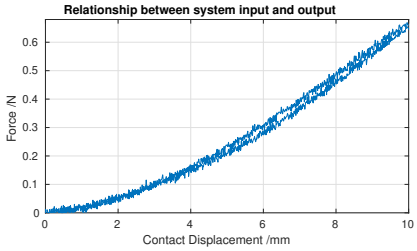

Fig. 10. Relationship between the distance and contact force.

For comparison purposes, two commonly-used system models are also built to represent the interaction, namely state space (SS) model and transfer function (TF) model. These two models are identified with the help of System Identification toolbox in MATLAB, where the order of the SS model is chosen in terms of the best goodness-of-fit automatically and the TF is designed with two zeros and two poles, i.e., a second-order system.

The estimated system outputs of three films using different models are shown in Fig. 11 and Table I. It is apparent that the linearized model based on Koopman operator accurately estimates the actual nonlinear system output with the smallest estimation errors. The root-mean-square error (RMSE) and the maximum absolute error (MaxAE) in the system estimation of the proposed method are much less than the SS model and TF model. In terms of RMSEs, the proposed method reduces 58.9% and 84.8% of the RMSEs than the SS model and the TF model, respectively. Also, the RMSE while using the proposed method dose not vary much for different soft films. Hence,

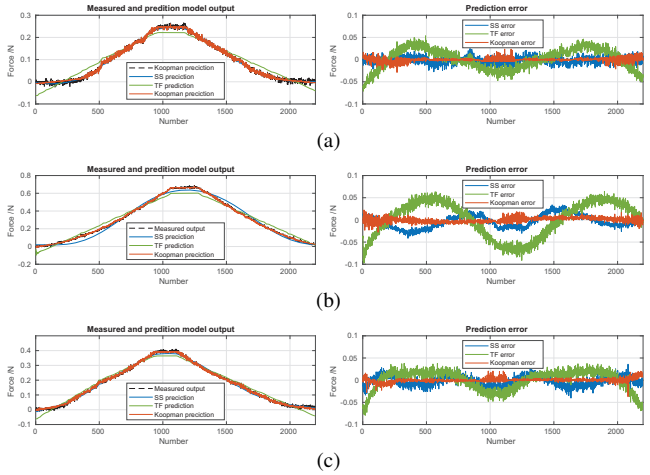

Fig. 11. Koopman operator-based modeling performance with different soft films: (a) thin film;(b) original film; (c) thick film.

TABLE I
PREDICTION OUTPUTS AND ERRORS FOR THREE DIFFERENT THICKNESSES OF MATERIAL.

Type	MaxAE			RMSE		
(unit: N)	SS	TF	Koopman	SS	TF	Koopman
Thin	0.0274	0.0711	0.0289	0.0080	0.0244	0.0048
Original	0.0414	0.0973	0.0276	0.0146	0.0394	0.0060
Thick	0.0403	0.0790	0.0371	0.0114	0.0221	0.0045

the proposed model can well represent the deformable object interaction accurately and robustly, which is also the most suitable model for the model-based controller design.

C. Contact Force Control

Several experiments are conducted to evaluate the performance and robustness of the proposed contact force control scheme. The $r(t)$ represents the desired contact force between the end of the cotton swab and the film in Newtons (N).

Furthermore, in all the experiments, two widely-used controllers, including a linear controller, proportional-integral-derivative (PID) controller, and a nonlinear controller, sliding mode controller (SMC), are used for comparison purpose.

The control law of the PID controller takes the form of

$$u_{PID} = K_P e + K_I \int_0^t e d\tau + K_D \frac{de}{dt}, \tag{13}$$

where K_P, K_I, and K_D are the PID controller parameters. The parameters are first calculated via the LQ control technique [6] based on the nominal linear model of the system and then fine tuned by the trial-and-error method.

The control law of the SMC controller takes the form of

$$u_{SMC} = \frac{1}{b_0}[\ddot{r} - f_0(x, \dot{x})] + K_1 e + K_2 \dot{e} + \varepsilon sign(s) + K_s s, \tag{14}$$

where b_0 is the parameter of the nominal model obtained by system identification, f_0 represents part of the nominal model, ε and K_s are the sliding mode controller parameters. $s = e + \lambda_1 \dot{e} + \lambda_2 \int e dt$ represents the sliding mode surface. To reduce the chattering effects due to the sign$(\cdot)$ function, the sat$(\cdot)$ function is used instead.

1) Sine Wave: At first, four different sine waves are used as the reference trajectory in the experiments. The trajectories can be represented by $\Lambda[1 - \cos(\omega t)]$, where Λ is the trajectory amplitude and ω is the trajectory frequency. The reason of choosing the $[1 - \cos(\cdot)]$ trajectory is to ensure that the robot does not move too fast at the beginning to avoid a huge change during the contact. These four trajectories are labelled as 'sine 1', 'sine 2', 'sine 3', and 'sine 4', where 'sine 1' is defined as normal amplitude and normal speed, 'sine 2' and 'sine 4' are with the same amplitude of 'sine 1' but 'sine 2' is with faster speed while 'sine 4' is with slower speed, and 'sine 3' is with the same speed of 'sine 1' but smaller amplitude.

Based on the modeling results presented in Section V-B, the system parameters $[A, B]$ can be obtained for the soft film after the model linearization process. Then, according to the calculation of K-LQ detailed in Section IV-B, the positive definite matrices Q, and R are selected to form the quadratic objective function J_2. By combining (10) and the lifting function, the control output u_{K-LQ} can be obtained.

Figure 12 and Table II show the experimental comparison results using the proposed K-LQ controller,the PID controller, and SMC, respectively (more results are illustrated in the video). It is clear that the K-LQ controller performs much better than the other two controllers. This is because the Koopman operator can well linearized the nonlinear system. Thus, it offers an accurate linearized model to apply the LQ technique (for linear system) which helps the LQ technique

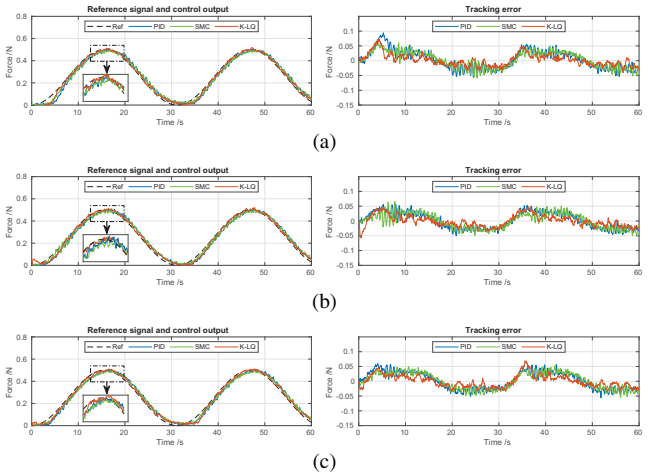

Fig. 12. Control performance on different soft films with different controllers with sine wave ('sine 1'): (a) thin film;(b) original film; (c) thick film.

TABLE II
COMPARISON OF CONTROL TRACKING ERRORS FOR THREE DIFFERENT THICKNESSES OF MATERIAL.

Type	Trajectory Type		MaxAE			RMSE		
			PID	SMC	K-LQ	PID	SMC	K-LQ
Thin	Sine	1	0.0943	0.0610	0.0729	0.0311	0.0277	0.0200
		2	0.1690	0.1303	0.1371	0.0554	0.0531	0.0435
		3	0.0968	0.0715	0.0704	0.0282	0.0254	0.0204
		4	0.0724	0.0731	0.0674	0.0271	0.0264	0.0216
	Triangle		0.1240	0.1037	0.1050	0.0407	0.0385	0.0325
Original	Sine	1	0.0559	0.0654	0.0572	0.0272	0.0250	0.0194
		2	0.0941	0.0960	0.1153	0.0503	0.0482	0.0381
		3	0.0575	0.0538	0.0496	0.025	0.0214	0.0182
		4	0.0479	0.0442	0.0466	0.0233	0.0212	0.0170
	Triangle		0.0770	0.0630	0.0657	0.0384	0.0366	0.0302
Thick	Sine	1	0.0598	0.0548	0.0696	0.0292	0.0274	0.0209
		2	0.0932	0.0871	0.1030	0.0508	0.0479	0.0407
		3	0.0471	0.0552	0.0720	0.0220	0.0201	0.0160
		4	0.0542	0.0575	0.0586	0.0229	0.0207	0.0173
	Triangle		0.0716	0.0750	0.0825	0.0393	0.0373	0.0312

to be still able to work well even though the system behaves strong nonlinearites.

Moreover, as can be seen from the results listed in Table II, the K-LQ controller performs much better tracking performance regardless of the soft film used. In terms of the RMSEs, the K-LQ controller at least reduce by 28% than the PID controller and 22% than the SMC for 'sine 1' trajectory. By considering all the sine trajectories and comparing with the SMC, the RMSEs using the K-LQ controller reduce by 18.16% to 27.89% for thin film, reduce by 15.35% to 22% for original film, and reduce by 14.80% to 27.10% for thick film. Also, the RMSE while using the K-LQ controller vary less for different soft films, which exhibits strong robustness of the proposed control system.

2) Triangle Wave: The system is further tested with a discontinuous trajectory, the triangle wave, as the reference trajectory. It should be noted that $\ddot{r}$ is set as 0 at the trajectory's change points for the SMC. Fig. 13 shows the tracking performance of different controllers with the triangle wave and Table II list the statistical analysis of the tracking errors. As can be seen, it is also clear that the proposed controller perform the best which RMSEs are at least 20% and 15% less than the PID controller and the SMC, respectively.

Thus, it can be concluded that the proposed control scheme can help the robotic system to achieve excellent force tracking performance and strong robustness in the interaction control

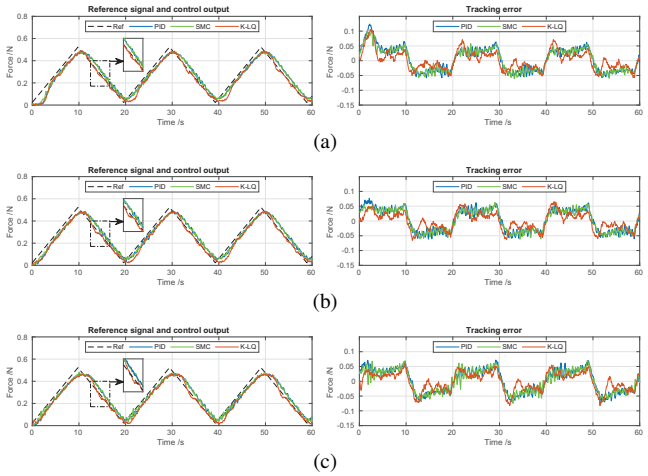

Fig. 13. Control performance on different soft films with different controllers with triangle wave: (a) thin film;(b) original film; (c) thick film.

on deformable objects.

VI. Conclusion

In this paper, a motion planning and interaction control framework using tactile feedback for achieving sensory-extended robotic interaction with deformable objects was proposed and developed. To address the challenges when a robot is required to be interacted with the deformable objects and/or in a vision-denied environment, an improved tactile sensor was designed and integrated into a robotic gripper. Moreover, inspired by the interaction task for swab test, the robotic system was designed to perform contact alignment planning and precision contact force control. For the alignment planning, a tactile-based classifier using QDA was implemented to estimate the contact angle. With the estimated contact angle, a manipulation planning process was then proposed to align the tool's pose to maintain a desired contact angle with the surface (in the case of swabbing, full contact is required). For the contact force control, a Koopman operator-based optimal control scheme using LQ technique was proposed.

Several experiments were conducted on three different soft films with different thicknesses. The experimental results show that the contact angle can be estimated correctly with a resolution of up to 1.5 deg and an accuracy of 98.4% as well as excellent tracking performance and strong robustness in the contact force control. It also shows that the proposed controller can achieve at least 19% and 14% improvement in terms of RMSE over the PID controller and the SMC, respectively. It would be great to extent to other types of deformable object manipulation as our future work. Regarding the improved GTac sensor using in this study, it would be interesting to quantitatively investigate the benefit of adding the FA-I layer buffer (Fig. 5) to the contact force control and the tasks relied on the tactile feedback as future work.

In summary, this research provides a solution and proof-of-concept on how to achieve a desired interaction with the deformable objects, especially without the visual information. It can be potentially extended to other deformable objects applied in the applications such as robotic swab test, robotic cleaning on soft surface, robotic pollination, etc.

References

[1] Y. Shen *et al.*, "Robots under COVID-19 pandemic: A comprehensive survey," *IEEE Access*, vol. 9, pp. 1590–1615, 2021.

[2] X. V. Wang and L. Wang, "A literature survey of the robotic technologies during the COVID-19 pandemic," *J. Manuf. Syst.*, vol. 60, pp. 823–836, 2021.

[3] S. Pondaven-Letourmy, F. Alvin, Y. Boumghit, and F. Simon, "How to perform a nasopharyngeal swab in adults and children in the COVID-19 era," *Eur. Ann. Otorhinolaryngology, Head and Neck Diseases*, vol. 137, no. 4, pp. 325–327, 2020.

[4] Z. Lu, X. Gao, and H. Yu, "GTac: A Biomimetic Tactile Sensor With Skin-Like Heterogeneous Force Feedback for Robots," *IEEE Sensors J.*, vol. 22, no. 14, pp. 14 491–14 500, 2022.

[5] Z. Lu *et al.*, "GTac-Gripper: A Reconfigurable Under-Actuated Four-Fingered Robotic Gripper With Tactile Sensing," *IEEE Robot. Autom. Lett.*, vol. 7, no. 3, pp. 7232–7239, 2022.

[6] W. Liang, J. Ma, and K. K. Tan, "Contact force control on soft membrane for an ear surgical device," *IEEE Trans. on Ind. Electron.*, vol. 65, no. 12, pp. 9593–9603, 2018.

[7] R. Wen *et al.*, "Force-guided high-precision grasping control of fragile and deformable objects using semg-based force prediction," *IEEE Robot. Autom. Lett.*, vol. 5, no. 2, pp. 2762–2769, 2020.

[8] A. Pappalardo *et al.*, "Hunt–crossley model based force control for minimally invasive robotic surgery," *Biomed. Signal Process. and Control*, vol. 29, pp. 31–43, 2016.

[9] T. Nanayakkara *et al.*, "Stable grip control on soft objects with time-varying stiffness," *IEEE Trans. on Robot.*, vol. 32, no. 3, pp. 626–637, 2016.

[10] Q. Ren *et al.*, "Learning-based force control of a surgical robot for tool-soft tissue interaction," *IEEE Robot. Autom. Lett.*, vol. 6, no. 4, pp. 6345–6352, 2021.

[11] B. O. Koopman, "Hamiltonian systems and transformation in hilbert space," *Proc. the Nat. Academy of Sciences*, vol. 17, no. 5, pp. 315–318, 1931.

[12] M. O. Williams, I. G. Kevrekidis, and C. W. Rowley, "A data–driven approximation of the koopman operator: Extending dynamic mode decomposition," *J. Nonlinear Science*, vol. 25, no. 6, pp. 1307–1346, 2015.

[13] Q. Li *et al.*, "Extended dynamic mode decomposition with dictionary learning: A data-driven adaptive spectral decomposition of the koopman operator," *Chaos: An Interdisciplinary J. Nonlinear Science*, vol. 27, no. 10, p. 103111, 2017.

[14] A. Mauroy and I. Mezić, "Global stability analysis using the eigenfunctions of the koopman operator," *IEEE Trans. on Autom. Control*, vol. 61, no. 11, pp. 3356–3369, 2016.

[15] S. Klus, P. Koltai, and C. Schütte, "On the numerical approximation of the Perron-Frobenius and Koopman operator," *J. Comput. Dyn.*, vol. 3, no. 1, pp. 51–79, 2016.

[16] I. Mezić, "On applications of the spectral theory of the Koopman operator in dynamical systems and control theory," in *CDC 2015*. IEEE, 2015, pp. 7034–7041.

[17] I. Abraham, G. De La Torre, and T. D. Murphey, "Model-based control using Koopman operators," in *RSS 2017*, 2017.

[18] S. Peitz and S. Klus, "Koopman operator-based model reduction for switched-system control of PDEs," *Automatica*, vol. 106, pp. 184–191, 2019.

[19] H. Wang *et al.*, "Robust position control of a continuum manipulator based on selective approach and Koopman operator," *IEEE Trans. on Ind. Electron.*, pp. 1–10, 2023.

[20] H. Shi and M. Q.-H. Meng, "Deep koopman operator with control for nonlinear systems," *IEEE Robot. Autom. Lett.*, vol. 7, no. 3, pp. 7700–7707, 2022.

[21] Smooth-On, Inc., "Dragon Skin™ 30 Product Information." [Online]. Available: https://www.smooth-on.com/products/dragon-skin-30/

[22] M. Griffin *et al.*, "Biomechanical characterisation of the human nasal cartilages; implications for tissue engineering," *J. Materials Science: Materials in Medicine*, vol. 27, no. 1, pp. 1–6, 2016.

[23] C. F. Guimarães, L. Gasperini, A. P. Marques, and R. L. Reis, "The stiffness of living tissues and its implications for tissue engineering," *Nature Reviews Materials*, vol. 5, no. 5, pp. 351–370, 2020.

[24] M. Athans and P. L. Falb, *Optimal control: An introduction to the theory and its applications*. Courier Corporation, 2013.